



PAPER • OPEN ACCESS

New insights into the laser produced electron–positron pairs

To cite this article: Hui Chen *et al* 2013 *New J. Phys.* **15** 065010

View the [article online](#) for updates and enhancements.

You may also like

- [Review of laser-driven ion sources and their applications](#)
Hiroyuki Daido, Mamiko Nishiuchi and Alexander S Pirozhkov
- [Dominance of hole-boring radiation pressure acceleration regime with thin ribbon of ionized solid hydrogen](#)
J Psikal and M Matys
- [Improvement of hot-electron and gamma-ray yields by selecting preplasma thickness for a target irradiated by a short laser pulse](#)
A.V. Brantov, M.G. Lobok and V.Yu. Bychenkov

New insights into the laser produced electron–positron pairs

Hui Chen^{1,4}, M Nakai², Y Sentoku³, Y Arikawa², H Azechi², S Fujioka², C Keane¹, S Kojima², W Goldstein¹, B R Maddox¹, N Miyanaga², T Morita², T Nagai², H Nishimura², T Ozaki², J Park¹, Y Sakawa², H Takabe², G Williams¹ and Z Zhang²

¹ Lawrence Livermore National Laboratory, Livermore, CA 94551, USA

² Institute of Laser Engineering, Osaka University, 2-6 Yamadaoka, Suita, Osaka 565-0871, Japan

³ Department of Physics, University of Nevada, Reno, NV 89557, USA

E-mail: chen33@llnl.gov

New Journal of Physics **15** (2013) 065010 (11pp)

Received 23 January 2013

Published 19 June 2013

Online at <http://www.njp.org/>

doi:10.1088/1367-2630/15/6/065010

Abstract. We report new results from the intense laser target interaction experiment that produces relativistic electron–positron pairs. Laser to electron energy transfer, inferred using x-ray and neutron measurements, was found to be consistent with the measured positrons. To increase the number of positrons, one needs to deliver a greater number of relativistic electrons from the laser–plasma interaction to the high Z gold target. A large preplasma was found to have a negative impact for this purpose, while the laser could produce hotter electrons in such preplasma. The peak energy shift in the positron spectrum is confirmed as the post-acceleration in the sheath potential behind the target. The results were supported by a collisional one-dimensional particle-in-cell code. This experiment was performed using the high-power LFEX laser at the Institute of Laser Engineering at Osaka University using a suite of diagnostics measuring electrons, positrons, x-rays and neutrons from the laser–target interaction at the relativistic regime.

⁴ Author to whom any correspondence should be addressed.



Content from this work may be used under the terms of the [Creative Commons Attribution 3.0 licence](https://creativecommons.org/licenses/by/3.0/). Any further distribution of this work must maintain attribution to the author(s) and the title of the work, journal citation and DOI.

Contents

1. Introduction	2
2. Experimental setup	3
3. Experimental results and discussions	4
4. Electron distributions	5
5. Positron measurement	7
6. Summary	9
Acknowledgments	10
References	10

1. Introduction

Rapid progress in laser technology in recent years is evident in the establishment of new facilities [1] near or at petawatt (10^{15} W) powers. Such facilities enable a number of physics applications to be studied including fast-ignition research for inertial confinement-fusion experiments [2, 3], proton beam generation and acceleration [4], MeV photon source development [5–7] and, recently, electron–positron antimatter production [8, 9]. Fast-electron beam generation and transport from relativistic laser-produced plasmas is the primary driver of these applications and has been the subject of a great deal of interest over the past decades. For example, fast electrons have been investigated using K- α spectroscopy [10, 11], K- α imaging [12, 13], bremsstrahlung measurements [14], nuclear activation [15] and direct measurement of escaping electrons [16]. The diagnostic capability to observe positrons produced from laser–plasma interactions has recently been added [17]. Positrons are produced most efficiently in thick targets through the Bethe–Heitler process [18] that begins with high-energy electrons generated from laser–target interaction. First, bremsstrahlung γ -rays are emitted by fast electrons, which are scattered in the field of high- Z nuclei. Then, an electron–positron pair is formed from the γ -ray photon decaying in the presence of a second nucleus. Positron signal, therefore, is a diagnostic aid in understanding the physics in relativistic laser–target interactions, albeit through multi-step processes. Intense laser-produced electron–positron pairs are interesting in their own right because they are a new source of positrons applicable to a variety of research disciplines including laboratory astrophysics, basic plasma science and antimatter research and applications [9]. Understanding the characteristics of laser-produced positrons and further optimizing their density and energy are the important preparatory steps toward the realization of these applications.

We performed an electron–positron generation experiment using the LFEX laser at the Institute of Laser Engineering at Osaka University. By observing electrons, positrons, x-rays and photoneutrons simultaneously, we investigated quantitatively the production processes of these high-energy particles and photons in the relativistic regime. From these measurements, we calculated the laser conversion to electrons and positrons. We also made correlation among electrons, positrons, K-shell x-rays and neutrons.

We found that very high-energy electrons ($T_{\text{hot}} \sim 10$ MeV) were produced from the LFEX experiments, indicating a large fraction of the laser pulse interacted with the long scale length plasma at under-critical density formed by a prepulse or energy pedestal on the main pulse.

Table 1. Summary of experimental results. The columns are (from left to right): shot number; on target laser energy E (in joules); temperature of hot electrons (from EPPS, in MeV) for electrons which had kinetic energy less (T_{hot1}) and greater (T_{hot2}) than 10 MeV; number of hot electrons from EPPS, $N(e)$, in number per sr; laser to hot-electron energy conversion efficiency, $\eta(e)$, inferred from Laue using EPPS data; number of total neutron, $N(n)$, measured from detector; number of high-energy photons, $N(\gamma)$, derived from the neutron diagnostic; energy conversion of high-energy photons, $\eta(\gamma)$; measured positron number, $N(e+)$, from EPPS; laser to EPPS positron conversion efficiency, $\eta(e+)$.

Shot	E (J)	I (W cm ⁻²)	T_{hot1} (MeV)	T_{hot2} (MeV)	$N(e)$	$\eta(e)$ (%)	$N(n)$	$N(\gamma)$	$\eta(\gamma)$ (%)	$N(e+)$	$\eta(e+)$ (%)
1	1675	1.2×10^{19}	1.8	16	8.2×10^{11}	15	8×10^8	1×10^{13}	0.2	2.3×10^{10}	0.003
2	1200	1×10^{19}	1.5	13	8.0×10^{11}	11	5×10^8	6×10^{12}	0.2	6.8×10^9	0.001
3	493	6×10^{18}	0.5	5	6.2×10^{10}	5	1×10^7	3×10^{11}	0.01	–	–
4	305	7×10^{18}	0.8	6.5	7.9×10^{10}	8	2×10^6	5×10^{10}	0.004	–	–
Titan	261	1.5×10^{19}	0.5	6	8.0×10^{11}	–	–	–	–	1.1×10^{10}	0.015

These observations are consistent with photoneutron measurements as well as particle-in-cell simulations using the PICLS code [19]. The inferred laser-to-electron conversion from x-ray measurement was 10–20%. This is somewhat less than that reported elsewhere [2, 10, 20]. Positrons were observed on two high-energy shots. The laser to positron energy conversion correlates with the laser to electron energy conversion. It also correlates with the laser to γ conversion. Finally, simulations show that the peak energy location in the positron spectra reflects the magnitude of the sheath potentials, a quantity critical to proton and positron acceleration, formed by the fast electrons transported through the massive target.

2. Experimental setup

The LFEX laser (www.ile.osaka-u.ac.jp/zone2/collab/facilities/A/LFEX_info.htm) has four beams, two of which were used during this experimental campaign. A laser pulse of duration 1–2 ps with a $1.053 \mu\text{m}$ wavelength was focused by an $f/11$ off-axis parabola to a focal spot of 40–50 μm resulting in a laser intensity of $1\text{--}2 \times 10^{19} \text{ W cm}^{-2}$ and a laser–plasma interaction in the relativistic regime. The intensity contrast ratio of the main pulse to the laser pedestal was about $10^6\text{--}10^8$, which leads to a relatively long (up to 10 μm) electron density scale length before the peak pulse arrives to the target [21]. The shot parameters are listed in table 1.

The diagnostic setup relative to the incident laser and target is shown in figure 1. The LFEX laser was aligned on the target (1 mm thick and 2 mm diameter gold discs) at 10° relative to the normal direction of the target. A Laue crystal spectrometer [22] was setup on the side of the laser, while the electron–positron proton spectrometer (EPPS) [23] and neutron diagnostics [24] were placed on the opposite side of the laser. The orientations of the diagnostic line of sights are marked in the figure. The Laue crystal spectrometer measures the gold characteristic K-shell radiation from which laser–electron coupling can be derived [25, 26]. All three types of diagnostics were absolutely calibrated prior to the experiment.

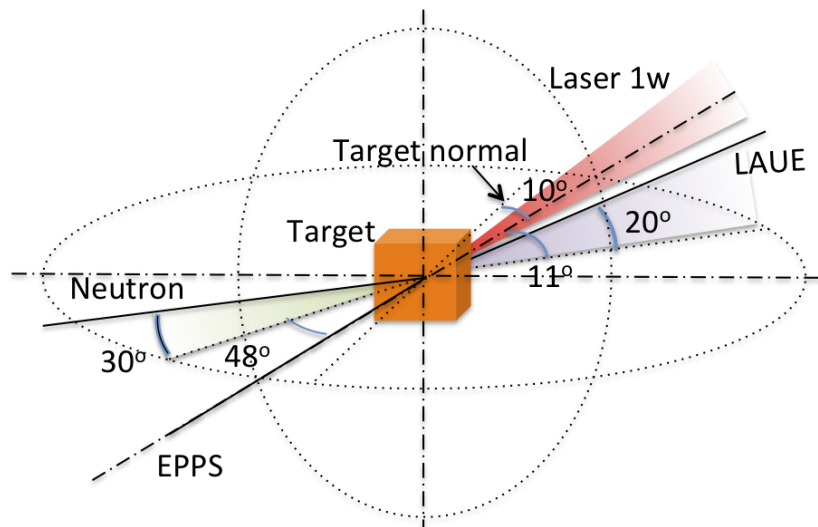


Figure 1. Diagnostic setup at LFEX laser.

The EPPS [23] measures the energy distribution of electrons and positrons between 1 and 100 MeV. Even though each EPPS has a finite solid angle, the total number of electrons and positrons can be estimated from the measured spectrum with the assumption that these particles have a Gaussian angular distribution at the back of the target with a full-width half-maximum (FWHM) of one solid angle. The assumption is based on our previous measurements that indicated that the FWHM of the electron and positron distribution was about 30–50° [8]. It is noted that the error associated with this assumption could be large (20–60%) for the absolute total particle numbers.

The neutron detectors [24] measure the number of neutrons with different energy threshold via photo nuclear reaction (γ, n) process. By analyzing the neutron flux, the high-energy electrons and bremsstrahlung photons can be estimated [27].

Both the Laue and EPPS diagnostics use image plates as a detector whose calibration was made with a GE image plate scanner. In this experiment, a GE model Typhoon FLA 7000 was used. To ensure that an absolute measurement could be derived from these diagnostics, we established the sensitivity calibration of this new scanner using a cross-calibrated radiocarbon source [28]. This process resulted in an empirical sensitivity conversion formula, allowing the scanner to operate at Fuji-equivalent sensitivity settings and permitting measured values to be directly compared with the results from the experiments in other laser facilities.

3. Experimental results and discussions

The experimental results are summarized in table 1 for shots taken at different laser energies and intensities. The laser intensity is averaged over the FWHM area of the focal spot. The targets were gold discs 1 mm thick and 2 mm in diameter. As a comparison, reference data taken at the Titan laser at the Lawrence Livermore National Laboratory are listed for the same target and laser intensity. Two hot-electron temperatures (T_{hot1} and T_{hot2}) are derived from the EPPS measurement for electrons. The total number of hot electrons from EPPS is obtained by integrating the whole measured spectrum with the angular distribution assumption described in

the previous section. More detailed discussions of the electron measurement and simulations are in the following section.

The laser-to-electron conversion efficiencies (η_e) are obtained from the Laue diagnostic measurements of gold K- α and K- β lines [22]. The K- α efficiency can be estimated by $\eta_{K\alpha} \propto \frac{\eta_e}{T_{\text{hot}}} \int_0^\infty dE \sigma_{K\alpha}(E) \int_0^d dx \frac{\exp(-E/T_{\text{hot}})}{T_{\text{hot}}} \exp(-\frac{x}{\lambda_{\text{mfp}} \cos \theta})$, where η_e is the laser transfer efficiency to electrons, $\sigma_{K\alpha}$ is the K-shell ionization cross-section, λ_{mfp} is the mean-free-path of K- α in the target and the hot-electron temperature is T_{hot} . The term $\exp(-\frac{x}{\lambda_{\text{mfp}} \cos \theta})$ describes the reabsorption of K α photons during the propagation through the target material where θ is the angle between the spectrometer and target normal. Following this model, the absolute K- α yield per solid angle was normalized to the laser energy, while $\eta_{K\alpha}$ was derived by the Laue spectrometer measurement. The laser–electron conversion was estimated [29] using the two-temperature (T_{hot1} and T_{hot2}) Maxwellian electron distribution from EPPS, an assumption of electron reflux [25], and the relativistic cross-section correction. The derived conversion efficiency was found to be proportional to laser intensity, but quantitatively less than that from the 30 to 50% reported previously [2, 10, 20].

The total number of neutrons produced from the experiment is between $\sim 10^6$ and 10^9 . Since these neutrons are generated primarily by photon–nuclei interaction, the shot-to-shot fluctuation in the neutron yield directly correlates with the distribution of high-energy photons and consequently the high-energy electrons. The neutron yield was estimated by using bubble neutron detectors BDS 1000 located 13 cm from the target. The γ -flux was calculated using a Monte Carlo simulation using electron spectrum measured by EPPS. In the calculation, it is assumed that only the (γ , 1n) reaction was significant: the number of the generated neutrons (N_n) is calculated from the spectral energy distribution of high-energy γ -photons (f) through a simple relation: $N_n = \int_0^t f(h\nu) \sigma_{\gamma n}(h\nu) d(h\nu)$, where $\sigma_{\gamma n}$ is the photon energy-dependent cross-section for the (γ , n) reaction and t the interaction length of the photon with the target. Cross-sectional data were taken from the JANDLE-4.0 library [30]. The background neutrons generated from EPPS, the wall of the vacuum chamber and bubble detector insertion mechanics were also calculated. Overall, about 60% of the neutron signal resulted using the Monte Carlo simulations from non-target components and the remaining 40(± 6)% of the signal was deemed to be from the target. The error in the analysis comes from the size of the components (the target, the target chamber, the EPPS and the bubble-detector-inserting-port) and the γ -ray spectrum. The total γ number and the energy-transfer efficiency inferred are listed in table 1.

Assuming a constant bremsstrahlung–positron cross-section (Bethe–Heitler process [18]), which is a reasonable assumption for the MeV photon energies, the conversion efficiency from photon to positron is about 1%. This is consistent (in order of magnitude) with the measured positron yield, considering that about 1% of the total produced positrons escape the target and are measured by EPPS [31].

4. Electron distributions

The fast electron distributions measured using EPPS are shown in figure 2. The electron spectra in figure 2 can be described in two distinctive regions: a lower temperature for the electrons at low energy (< 10 MeV) and a high temperature for the electrons at high energy (> 10 MeV). Although EPPS measured only for the electrons that escaped the targets, its distribution, especially those at high energies, reflects the electron spectrum produced by laser–target

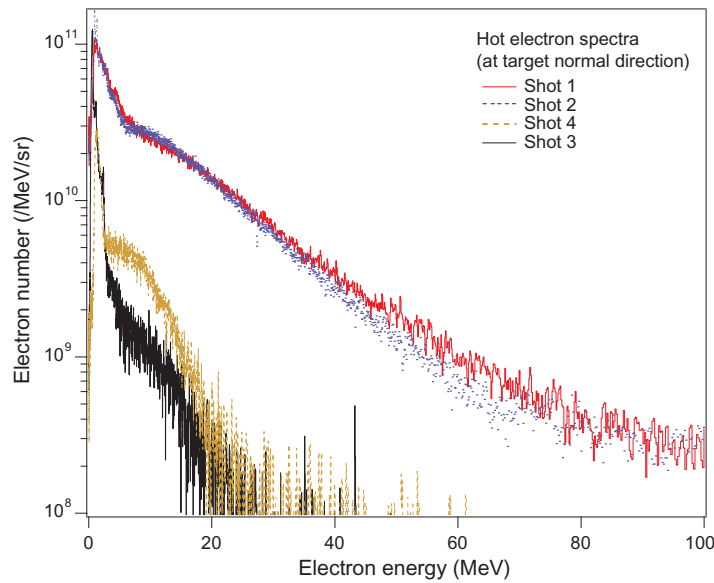


Figure 2. LFEX electron spectra measured by EPPS.

interaction [32, 33]. At low energy (< 10 MeV) where the electrons energies are equal to or less than the sheath potential, it is still a topic of debate as to the precise correlation of the number of escaping electrons to total number produced by lasers [32, 33].

The electron temperatures T_{hot2} are much higher than that of the intensity scaling. For example, for a laser intensity of $2 \times 10^{19} \text{ W cm}^{-2}$, the electron temperature is ~ 1 MeV according to the ponderomotive scaling [34], 0.6 MeV in Beg scaling [11] and Haines scaling [35]. These fast electrons were accelerated from under critical density plasma by the lasers possibly through mechanisms described in [36–39].

For a comparison, an electron spectrum observed on the Titan laser for the same laser intensity is also shown in figure 3. The Titan electron spectrum appears to have a much cooler energy distribution relative to that of LFEX. This may be due to the differences in laser contrast and possibly in the focusing parabola aspect ratio ($f/3$ on Titan and $f/11$ on LFEX) in two lasers.

As listed in table 1, the ratios of the measured electron energy to laser energy were about $1\text{--}2 \times 10^{-3}$ on both the LFEX and Titan lasers. The laser to electron coupling efficiency was 10–15% for the LFEX experiment. Although this parameter was not measured for the Titan experiment presented here, separate experiments on Titan indicated the laser–electron coupling efficiency was between 30 and 40% [14]. The total number of electrons from the LFEX experiments was about the same as that from Titan, but the ratio of electron number at energy about 10 MeV relative to the laser energy on LFEX was about 10% that of Titan.

To better understand the LFEX data, we performed one-dimensional particle-in-cell simulations using the PICLS code [19] for the LFEX and Titan laser conditions. We prepared a gold target with 1 mm thickness with a preplasma in front of the target. Since the LFEX laser has a slightly higher prepulse level than that on the Titan laser, we initialized the simulation by placing a preplasma with a $10 \mu\text{m}$ scale length for the LFEX laser [21] and a few μm scale length for the Titan laser [40]. The simulation contained all relevant physics regarding the transport in the high- Z gold target, including Coulomb collisions [19], impact ionization

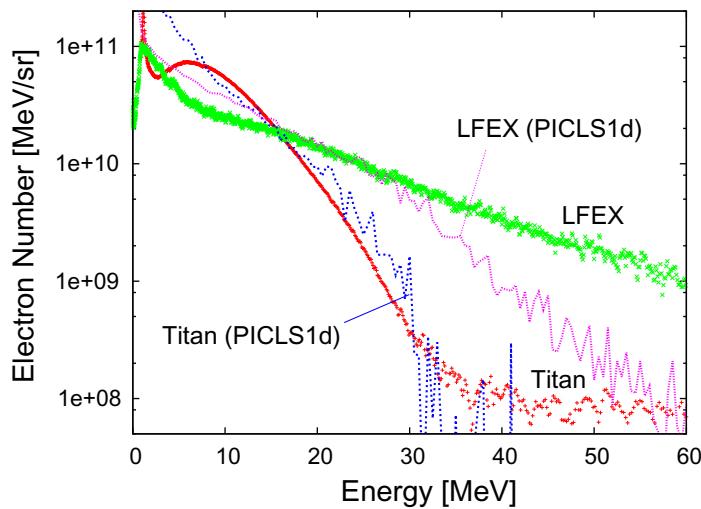


Figure 3. Comparison of electron spectrum from LFEX and Titan and PICLS simulations.

and bremsstrahlung radiation [41]. The details of the ionization model have not been published yet; however, it has been benchmarked against the transport experiments in gold targets [40, 42]. The laser duration was set to 2 ps for LFEX and 700 fs for Titan. The total simulation time was about 24 ps, which is long enough to see the electrostatic potential evolution at the target surface and energy transport and decay in the gold target. The spatial and temporal resolution of the simulation was 40 nm and 0.132 fs (25 time steps for one laser period), respectively. This resolution is sufficient to simulate laser absorption, fast electron transport and sheath excitation at the target surface. The kinetic phenomena for cold electrons such as the Debye screening and wave excitation are under-resolved; however, they are not important due to the high resistivity in the gold target [19]. We keep the input laser energy ratio between two pulses similar with the experiments at ~ 6 . The peak laser intensity is set to $2 \times 10^{19} \text{ W cm}^{-2}$ for the Titan laser and $4 \times 10^{19} \text{ W cm}^{-2}$ for the LFEX laser, which is higher than the experimental ones. The higher intensity is introduced to compensate for one-dimensional limitations, namely the lower absorption due to lack of multi-dimensional effects such as self-focusing and/or filamentation. Note here that after performing a number of simulations by changing the laser conditions, we find that the hot electron spectrum is closer to the experimental data when we use the measured laser energy instead of laser intensity. Nevertheless, the purpose of these simulations is to compare these two laser systems on the basis of hot-electron production, sheath potential created at the back surface of the gold target and the resulting effect on the positron spectra.

Figure 3 shows the hot-electron spectra observed in both experiments and simulations. Note here that the experiments see only the escaping electrons and simulations show all hot electrons inside the target at the time when the laser pulse is over.

5. Positron measurement

Positron data were obtained for the two high laser energy shots (#1 and #2) on the LFEX experiment, as listed in table 1. For the two low-energy shots (#3–#4), the positron signals were too weak to allow any quantitative measurement. A comparison of positron spectra taken

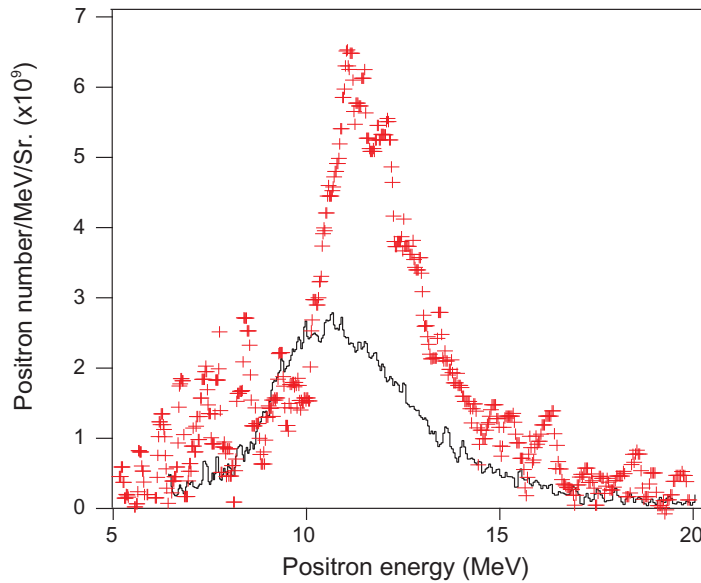


Figure 4. Positron spectra measured on LFEX (cross) and Titan (line). The laser parameters for the two shots are listed in table 1.

from LFEX (for shot #1) and Titan for equivalent laser intensity of $2 \times 10^{19} \text{ W cm}^{-2}$ is shown in figure 4. Although a factor of 2 was found between the number of pairs detected, the positron conversion (defined as integrated positron energy divided by the laser energy) is 3.1×10^{-5} and 1.5×10^{-4} for LFEX and Titan, respectively.

Precise physical reason behind such differences is not yet clear, although we could make some deductions based on the data. LFEX-laser energy was about a factor of 5 higher than that in Titan, but the laser to electron conversion efficiency is a factor of 2–3 less. Therefore, we infer that the total number of electrons generated in the LFEX experiment is only about twice as much as that from Titan, which is consistent with the fact that the LFEX laser produces about twice the number of positrons than that of Titan.

As stated above, we observed hotter electron distributions from the LFEX experiment. The reason as to why the hotter electron distribution does not appear to enhance the pair generation is not known. Although the electron distribution is cooler on Titan, it seemed to have more of the lower energy ($\sim 10 \text{ MeV}$) electrons. Based on the simulations, the LFEX laser heated the large preplasma and produced a large electrostatic potential ($\sim 10 \text{ MV}$) at the absorption point. This potential accelerates the ions to the forward direction, called the collisionless shock acceleration, but slows down the fast electrons. In a multi-dimensional scenario, not only the electrostatic potential but also the strong magnetic fields are generated, and they act as a gate of lower energy electrons. This is the reason why the LFEX experiment injected a smaller number of lower energy electrons into the target. Therefore, we expect the higher efficiency of the positron production on the LFEX laser by reducing the preplasma, or improve the contrast ratio, to make the pulse directly interact with the target. Optimization of target thickness for various temperature electrons has been previously studied in [43, 44].

The LFEX positron distribution was centered at $\sim 12 \text{ MeV}$. Positron creation spectrum is typically 1–3 MeV when produced by the Bethe–Heitler processes [45]. When pulse intensity increases, we expect that the peak could shift to the higher energy. For the laser intensities

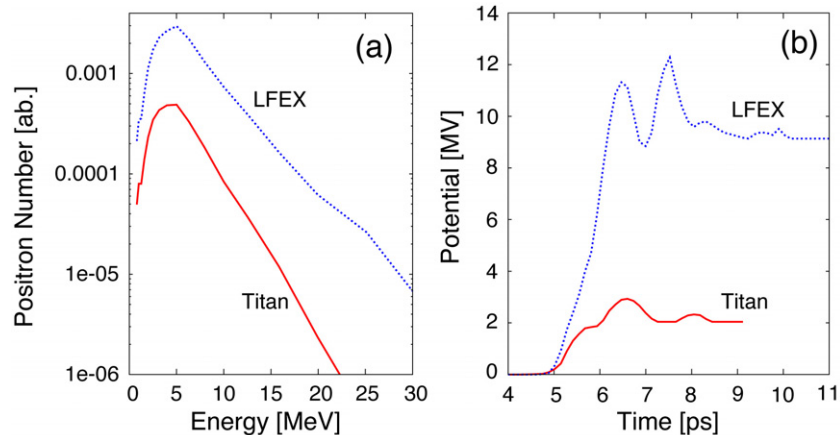


Figure 5. (a) Positron spectrum calculated from the γ -rays spectrum in PICLS simulation at the end of the simulation. (b) Time evolution of the electric potentials at the target backside in the simulations.

discussed here, the peak appears at around 5 MeV as shown in figure 5(a). These positron spectra are calculated from the bremsstrahlung γ -ray spectra using the cross section of the Bethe–Heitler processes without taking into account the transport dynamics. The peak shift of the positron spectrum is explained by the sheath acceleration at the back of the target [8]. As shown in figure 5(b), the PIC simulations show the onset of a sheath potential for the LFEX laser with a magnitude of 10 MV, whereas the Titan laser a few MV. These potential values could explain the peak shift of positron spectra observed in experiments. The potential of the resistive field inside the target with the LFEX parameter is about $\text{kV } \mu\text{m}^{-1}$, which is MV through the target, that is, it is not strong enough to explain the shift of positrons energy. Note here that the electron recirculation is not important in this massive gold target with a thickness of 1 mm, where an electron takes 6 ps for one round trip. The potential oscillation is attributed to the laser absorption processes which occurred in a long-scale preplasma [46].

6. Summary

We reported the results of first electron–positron experiment on the LFEX laser where x-ray, neutron, electron and positrons were measured simultaneously. Consistencies were found among different diagnostics for the coupling efficiency of laser to electrons and laser to positrons. Measured electron spectra show that very high-energy electrons ($T_{\text{hot}} \sim 10 \text{ MeV}$) were produced, indicating an intense laser pulse interacted with a long scale length pre-plasma at under-critical density, which was confirmed by particle-in-cell simulations. In addition, our simulations show that the shift of positron energy spectrum is proportional to the sheath potentials. However, detailed quantitative correlations among the positron, bremsstrahlung and electron data are highly complex due to its large scale (mm interaction length and 10 s of picoseconds interaction time). Additional large scale, multi-dimensional modeling efforts are needed to provide a more complete picture to better understand the experiment.

Acknowledgments

The authors would like to thank the anonymous referees for their critical comments. We gratefully acknowledge the support of the GEKKO XII operation group, the LFEX development and operation group and the plasma diagnostics operation group of the Institute of Laser Engineering, Osaka University. This work was performed under the auspices of the US DOE by LLNL under contract DE-AC52-07NA27344 and LDRD (no. 12-ERD-062), and partially funded by ILE's Joint Research Program.

References

- [1] Dunne M *et al* 2007 *HiPER Technical Background and Conceptual Design Report 2007* www.hiperlaser.org/
- [2] Key M H 2007 *Phys. Plasmas* **14** 055502
- [3] Kodama R *et al* 2001 *Nature* **412** 798
- [4] Roth M *et al* 2001 *Phys. Rev. Lett.* **86** 436
- [5] Edwards R D *et al* 2002 *Appl. Phys. Lett.* **80** 2129
- [6] Norreys P A *et al* 1999 *Phys. Plasmas* **6** 2150
- [7] Courtois C *et al* 2009 *Phys. Plasmas* **16** 013105
- [8] Chen H *et al* 2010 *Phys. Rev. Lett.* **105** 015003
- [9] Chen H *et al* 2011 *High Energy Density Phys.* **7** 225
- [10] Wharton K B, Hatchett S P, Wilks S C, Key M H, Moody J D, Yanovsky V, Offenberger A A, Hammel B A, Perry M D and Joshi C 1998 *Phys. Rev. Lett.* **81** 822
- [11] Beg F N, Bell A R, Dangor A E, Danson C N, Fews A P, Glinsky M E, Hammel B A, Lee P, Norreys P A and Tatarakis M 1997 *Phys. Plasmas* **4** 447
- [12] Stephens R B *et al* 2004 *Phys. Rev. E* **69** 066414
- [13] Ma T *et al* 2012 *Phys. Rev. Lett.* **108** 115004
- [14] Chen C D *et al* 2009 *Phys. Plasmas* **16** 082705
- [15] Cowan T E *et al* 2000 *Phys. Rev. Lett.* **84** 903
- [16] Chen H, Wilks S, Kruer B, Patel P K and Shepherd R 2009 *Phys. Plasmas* **16** 020705
- [17] Chen H, Wilks S, Patel P and Shepherd R 2006 *Rev. Sci. Instrum.* **77** 10E703
- [18] Bethe H A and Heitler W 1934 On the stopping of fast particles and on the creation of positive electrons *Proc. R. Soc. Lond. A* **146** 83
- [19] Sentoku Y and Kemp A J 2008 *J. Comput. Phys.* **227** 6846
- [20] Nilson P M *et al* 2011 *Phys. Plasmas* **18** 056703
- [21] Ohira S, Fujioka S and Sunahara A *et al* 2012 *J. App. Phys.* **112** 063301
- [22] Zhang Z *et al* 2012 *Rev. Sci. Instrum.* **83** 053502
- [23] Chen H, Link A J, van Maren R, Patel P K, Shepherd R, Wilks S C and Beiersdorfer P 2008 *Rev. Sci. Instrum.* **79** 10E533
- [24] Rosenstock W, Schulze J, Köble T, Kruzinski G, Thesing P, Jaunich G and Kronholz H L 1995 *Radiat. Prot. Dosim.* **61** 133
- [25] Myatt J, Theobald W, Delettrez J A, Stoeckl C, Storm M, Sangster T C, Maximov A V and Short R W 2007 *Phys. Plasmas* **14** 056301
- [26] Zulick F J *et al* 2011 *Can. J. Phys.* **89** 647
- [27] Günther M M, Sonnabend K, Brambrink E, Vogt K, Bagnoud V, Harres K and Roth M 2011 *Phys. Plasmas* **18** 083102
- [28] Williams G J, Maddox B R, Chen H, Kojima S, Millecchia M, Rowland M, Sorce C, Stone G F and Walker D 2013 *Rev. Sci. Instrum.* in preparation
- [29] Zhang Z *et al* 2012 APS/DPP: DPP12-2012-000856
- [30] Shibata K *et al* 2011 JENDL-4.0: a new library for nuclear science and engineering *J. Nucl. Sci. Technol.* **48** 1

- [31] Chen H *et al* 2009 *Phys. Rev. Lett.* **102** 105001
- [32] Cottrill L A, Kemp A, Tabak M and Town R P J 2010 *Nucl. Fusion* **50** 095002
- [33] Link A, Freeman R R, Schumacher D W and Van Woerkom L D 2011 *Phys. Plasmas* **18** 053107
- [34] Wilks S C, Kruer W L, Tabak M and Langdon A B 1992 Absorption of ultra-intense laser pulses *Phys. Rev. Lett.* **69** 1383
- [35] Haines M G, Wei M S, Beg F N and Stephens R B 2009 *Phys. Rev. Lett.* **102** 045008
- [36] Pukhov A and Meyer-ter-Vehn J 1999 *Phys. Plasma* **6** 2847
- [37] Naseri N, Bochkarev S G and Rozmus W 2010 *Phys. Plasma* **17** 033107
- [38] Arefiev A V, Breizman B N, Schollmeier M and Khudik V N 2012 *Phys. Rev. Lett.* **108** 145004
- [39] Willingale L, Nilson P M, Thomas A G R, Bulanov S S, Maksimchuk A, Nazarov W, Sangster T C, Stoeckl C and Krushelnick K 2011 *Phys. Plasma* **18** 056706
- [40] Chawla S *et al* 2013 *Phys. Rev. Lett.* **110** 025001
- [41] Sentoku Y, Mima K, Taguchi T, Miyamoto S and Kishimoto Y 1998 *Phys. Plasmas* **5** 4366
- [42] Sentoku Y, d'Humieres E, Romagnani L, Audebert P and Fuchs J 2011 *Phys. Rev. Lett.* **107** 135005
- [43] Henderson A, Liang E, Yepes P, Chen H and Wilks S 2011 *Astrophys. Space Sci.* **295** 273
- [44] Yan Y, Wu Y, Zhao Z, Teng J and Yu J *et al* 2012 *Phys. Plasmas* **19** 023114
- [45] Nakashima K and Takabe H 2002 *Phys. Plasmas* **9** 1505
- [46] Kemp A J, Sentoku Y and Tabak M 2008 *Phys. Rev. Lett.* **101** 075004